The Effect of the Marginal Ice Zone on the Directional Wave Spectrum of the Ocean

PETER WADHAMS AND VERNON A. SQUIRE

Scott Polar Research Institute, University of Cambridge, Cambridge CB2 1ER, England

J. A. EWING AND R. W. PASCAL

Institute of Oceanographic Sciences, Wormley, Godalming, Surrey GU8 5UB, England

(Manuscript received 15 July 1985, in final form 1 October 1985)

ABSTRACT

During the MIZEX-84 experiment in the Greenland Sea in June–July 1984, a cooperative program was carried out between the Scott Polar Research Institute (SPRI) and the Institute of Oceanographic Sciences (IOS) to measure the change in the directional character of the ocean wave spectrum in the immediate vicinity of the ice edge. The aim was to extend one-dimensional spectral measurements made hitherto so as to study in full the processes of reflection and refraction. Directional spectrum analysis of these records shows that (i) significant reflection of wave energy occurs at the ice edge (detected using Long-Hasselmann analysis); (ii) within the ice the directional spectrum at high frequencies, where attenuation is rapid, broadens to become almost isotropic; whereas (iii) the directional spectrum at swell frequencies, where the attenuation is slower, becomes initially narrower before broadening more slowly than the high frequency energy. An explanation of these effects is offered in terms of scattering theory, which also gives a good fit to the observed rates of attenuation within the ice.

1. Introduction

When a train of ocean waves enters a marginal ice zone (MIZ) composed of discrete floes, the wave energy is progressively attenuated with increasing penetration into the ice field. Wadhams (1973, 1975, 1978) showed that in a homogeneous ice field the decay is exponential, i.e., of form

$$E(x) = E(0)\exp(-\lambda x), \tag{1}$$

where x is penetration and λ increases with frequency. Wadhams (1973, 1986) also showed that a model based on scattering of wave energy by floes gives predictions of λ which agree well with field experiments. The limitations of this model are, first, that it describes only one-dimensional energy decay along the axis of propagation of the wave. Although it predicts the reflection coefficient of floes (interpreted as an attenuation of the transmitted wave) it does not deal with the subsequent history of the reflected wave components nor the components scattered at other angles, and so it does not treat the directional form of the spectrum within the ice field nor the form of the scattered spectrum emerging from the ice edge when a wave train enters the ice. The model assumes that although the dispersion relation is modified under an ice floe, the transmitted wave is parallel to the incident wave, so that the ice field as a whole does not cause an obliquely incident wave train to be refracted at the ice edge.

On the basis of this simple model we might guess that there is no refraction at ice edges; that reflection occurs in the form of backscattering so that the reflected spectrum can be predicted from the reflection coefficient of the first row or two of ice floes encountered; and that the directional spread of a spectrum may become narrower within an ice field and more closely concentrated along a bearing normal to the ice edge. This last suggestion, made by Wadhams (1978), is based on the idea that at any distance x from the ice edge, wave components with an angle of incidence θ will have travelled a distance ($x \sec\theta$) through ice and will therefore have suffered an attenuation which increases with θ. At deep penetrations we might then expect a spectrum to be almost unidirectional, propagating at right angles to the mean orientation of the local ice edge.

There is no published experimental evidence for refraction at MIZ ice edges, although there is anecdotal evidence from inspection of SAR (synthetic aperture radar) images that refraction occurs at the ice edge in the Greenland Sea (O. H. Shemdin, D. B. Ross, personal communication, 1985). These images were obtained during the 1979 NORSEX experiment and 1983 MIZEX pilot study. Refraction at other types of ice edge has been described theoretically: waves entering a continuous fast ice sheet are refracted because they propagate onwards as flexural-gravity waves with altered dispersion (Squire, 1984); while waves entering

a field of frazil ice are refracted because the surface loading by the ice particles also alters the dispersion relation (Weitz and Keller, 1950; Wadhams, 1973, 1986). No published directional spectra have been obtained within or near ice edges.

Waves at the ice edge are also thought to be important in the generation and maintenance of ice edge bands. Bands are distinct features several kilometers long and a few hundred meters wide, which are observed to form under off-ice wind conditions (Martin et al., 1983) and which may be partly driven by wave radiation pressure (Wadhams, 1983).

The present experiments were conducted in the northern Greenland Sea during July 1984 from the sealer M.S. *Kvitbjørn* as part of the MIZEX-84 programme (Johannessen and Horn, 1984; Wadhams, 1985). A directional wave buoy was deployed outside and just inside the ice edge, and a package of accelerometer and tiltmeters was placed on floes to record the directional nature of waves deeper within the ice. In this way it has been possible to obtain the first measurements of the directional behavior of wave fields near ice margins. Some preliminary results have been reported by Wadhams et al. (1985); we here report the complete results of the experiments.

2. Description of experiments

The measurements were made along the east Greenland ice edge region between 78° and 80°N. The typical trend of the ice edge in the region was NE–SW. The experiments were of three types:

1) Single-station experiments in support of overflights by aircraft equipped with synthetic aperture radar and laser profiling equipment. Some of these were done earlier in MIZEX-84 by SPRI personnel from the German icebreaker *Polarstern*. Results will not be reported in this paper.

2) Sequences of observations along a line running into or out of the ice edge. The normal observation period per station was 34 minutes. Table 1 summarizes the four main experiments of this type.

3) Band experiments, where the buoy was deployed to windward and leeward of ice edge bands. Experiments of this kind were carried out on 10 and 11 July, to test the hypothesis of wave driving of bands.

The equipment used in open water comprised an IOS pitch–roll buoy (Ewing and Pitt, 1982), loosely tethered to the ship by approximately 100 m of buoyant power cable, which also carried data from the wave sensors to a magnetic tape recorder aboard ship. In the deployment of the buoy, care was taken to avoid situations where the ship shielded the buoy from the waves, or the possibility of wave reflection off the ship's side. The pitch–roll buoy has a diameter of 1.2 m and so provides information on waves up to at least 0.5 Hz in frequency. Deeper inside the ice field, where the waves were too small for the buoy to respond, a package was deployed directly on the ice floes to measure their bodily response in heave, pitch and roll. This may be assumed equivalent to the local water wave spectrum at long periods. The package consisted of a vertically-mounted Schaevitz accelerometer which sat on gimbals, two orthogonal electrolytic tiltmeters manufactured by TILT Measurement Ltd., and a compass. The tiltmeters were initally deployed in a N–S, E–W configuration. As the ice floe rotated during each experiment the compass gave a reference by which the tiltmeters could be related to their start position. The compass is believed to be accurate to ±5°, the tiltmeter calibrations to about 3% due to their strong dependence on temperature and linearity error, and the accelerometer calibration to about 0.1%. The tiltmeters discriminate 0.1 arc seconds, while the accelerometer discrimination was beneath the resolution of our measuring system. The three channels of data were recorded on a TOA chart recorder running at 80 mm min^{-1} and optimum gain. These records were later manually digitised before transfer to an IBM 3081 mainframe computer for preprocessing and spectral analysis.

3. Station configuration

a. Attenuation experiments

1) 8–9 JULY (RUN A)

The first experiment designed to measure the variation in the wave spectrum with distance from the ice

TABLE 1. Details of the directional wave experiments carried out from *Kvitbjørn* during MIZEX-84.

Date	8–9 July (Run A)	12–13 July (Run B)	13 July (Run C)	21 July (Run D)
Number of stations	7	9	7	5
Distance from edge, km (neg ⇒ within ice)	37.1, 27.8, 9.6, 6.3, 0.7, −4.1, −7.2	−22.5, −17.8, −11.2, −5.6, 8.2, 18.0, 21.1, 40.3, 73.0	19.9, 9.1, 4.2, 1.8, 1.2, 0, −1.2	1.1, 1.2, 5.0, 10.1, 22.2
Geometry of run	NW into ice	E out of ice	N into ice	S away from ice
Wind direction and speed	directly off-ice 300°, 4–7 m s^{-1}	obliquely on-ice 180°, 4–5 m s^{-1}	obliquely on-ice 200°, 4–6 m s^{-1}	directly on-ice 160°, 4 m s^{-1}

edge began with a station 37.1 km outside the ice edge at 2050 GMT 8 July (Fig. 1). A wind of 4–7 m s^{-1} from 300° was blowing directly off the ice, generating a young choppy sea of low fetch, on which an opposing swell appeared to be superimposed. The first five stations (0801 to 0903) consisted of 34-min recordings with the IOS buoy. Station 0903, begun at 0350 GMT 9 July, lay just outside the ice edge itself. From 0901 onwards the ice edge was within radar range and was plotted from the X-band PPI screen. As shown in Fig. 1, there is a variation in ice edge position between stations. This is partly due to the real motion of the ice edge, partly to errors in the ship's position given by the satellite navigator, and partly due to the fact that the same field of ice floes when viewed on different bearings presents different facets as strong radar reflectors so that the "edge" appears to change shape. Station 0904 lay 4.1 km inside a loose pack composed mainly of first-year floes of typical thickness 2.5 m and typical diameter 250 m. At this station the IOS buoy was floated alongside the ship in a polynya while the SPRI heave–tilt sensor was deployed on an ice floe. The final station, 0905, was accomplished in close pack in which the IOS buoy could not be put out, so only the SPRI heave–tilt sensor was deployed. As can be seen from Fig. 1, the time delay between stations, particularly that involved in working into ice, allows the possibility of the local wave spectrum changing due to a change in the duration of the wind.

2) 12–13 JULY (RUN B)

The second experiment was a run eastward out of the ice (Fig. 2) beginning in heavy pack. At station 1201 the SPRI heave–tilt sensor was deployed on a floe of 350 m diameter. Station 1202 was also a heave–tilt station in similar pack carried out on a 200 m floe. Station 1203 was in lighter pack near the edge; the heave–tilt sensor was inoperative, so a heave sensor alone was deployed on a 72 m floe of thickness 3 m. Station 1301 was also a heave station on a heavily rotted floe in 1/10 ice cover. East of 1301 the ice became more compact (8/10) in the vicinity of the extreme edge, whose trend was about 020° according to radar. Stations 1302 to 1306 were IOS buoy stations in open water. The wind was blowing at 4–5 m s^{-1} from the south.

3) 13–14 JULY (RUN C)

The third experiment was a northward run into the pack (Fig. 3), with a following wind. The wind direction during the sequence of stations was relatively steady, with measurements varying from 187° to 219° (mean 205°), while the speed increased from 4.1 m s^{-1} at station 1307 to a mean of 6.0 m s^{-1} for the remaining stations. The ice stations were carried out in a tongue of ice associated with an eddy, so that the open water stations (1307–9, Fig. 3a) had ice quite close by to the

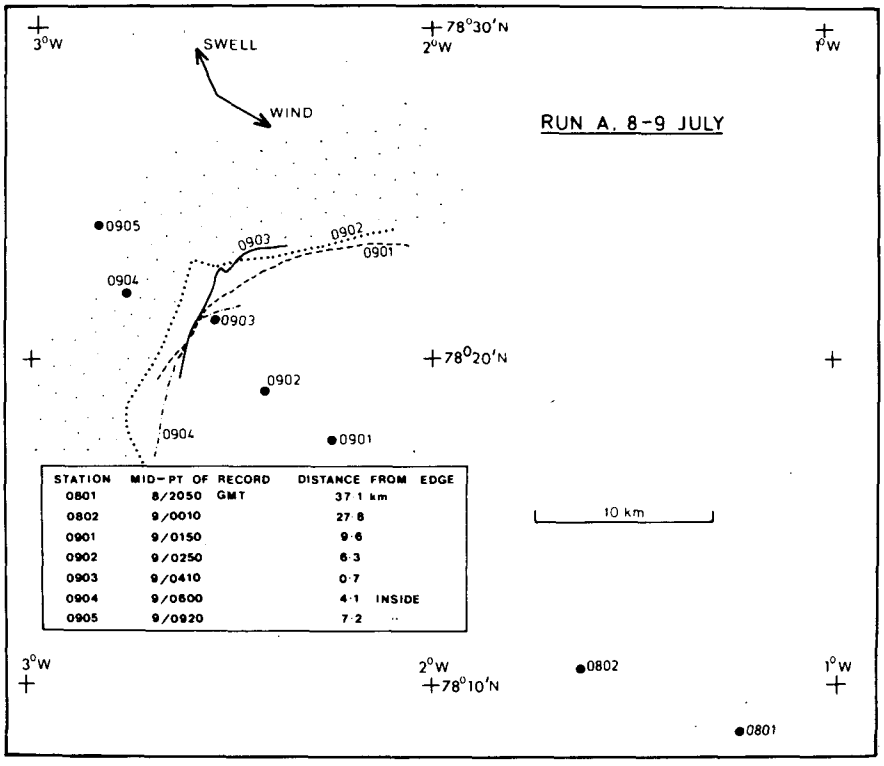

FIG. 1. Wave station positions for run A.

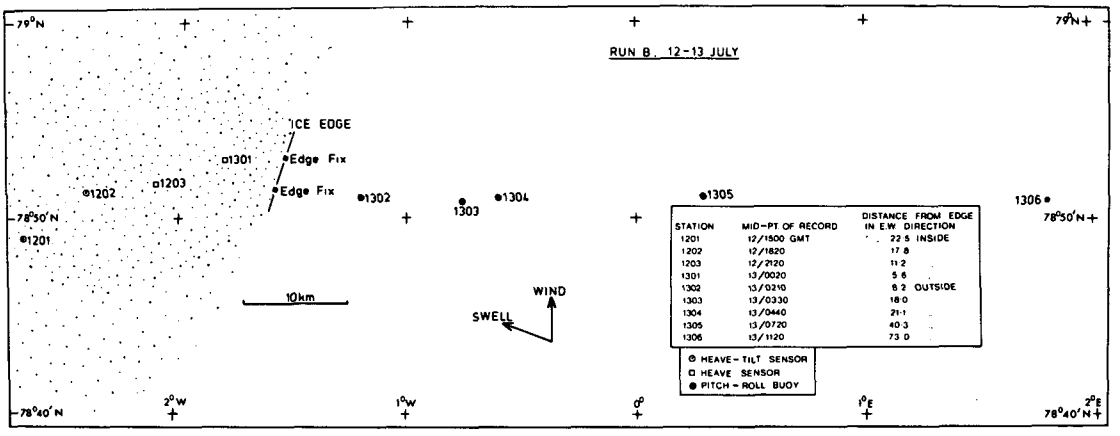

FIG. 2. As in Fig. 1 but for run B.

westward. Figure 3a shows the radar ice edge as seen relative to station 1308, while Fig. 3b, on a larger scale, shows the ice edges plotted relative to the later stations; again the ice edge movement is partly real and partly the result of navigational error. Stations 1307 to 1401 were done with the IOS buoy. 1403 was just outside the edge, but lay to leeward of a few small cakes which had some effect in damping down waves; 1404 was well within the ice, which formed an approximately 70% cover with typical floe diameter 80 m.

4) 21 JULY (RUN D)

The final experiment of this type (Fig. 4) was a southward run away from the ice edge with all stations being in open water. Five IOS buoy stations were performed. A few scattered floes existed outside the ice edge in the vicinity of stations 2101 and 2102. The wind direction was towards the ice, at 156° and 4 m s^{-1}. The main trend of the ice edge near the first two stations was E-W, forming the southern side of a tongue, and no ice lay within radar range to westward of the line. The run was carried out within a relatively short time interval (5 hours) so that spectral variations might be expected to relate mainly to distance from the ice edge rather than to change in wind duration.

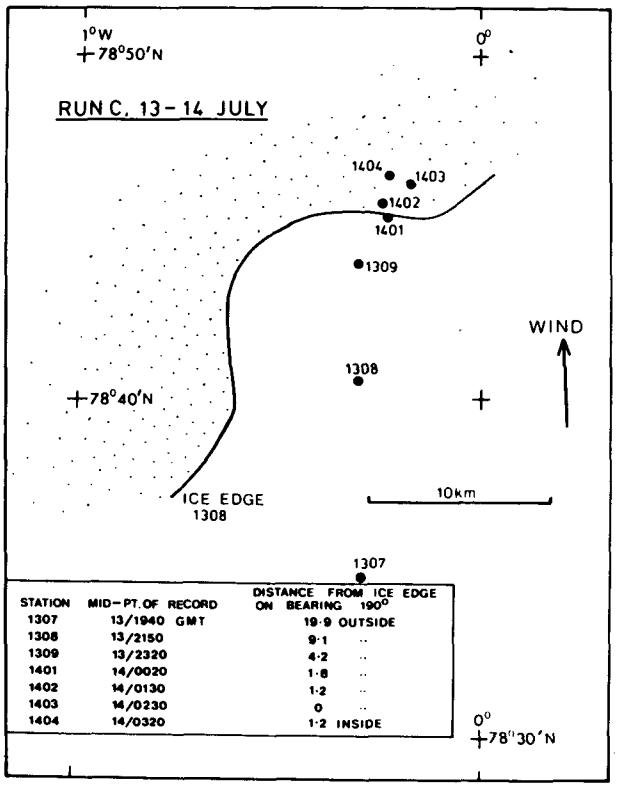

FIG. 3a. Wave station positions for run C. Ice edge is at position observed relative to station 1308.

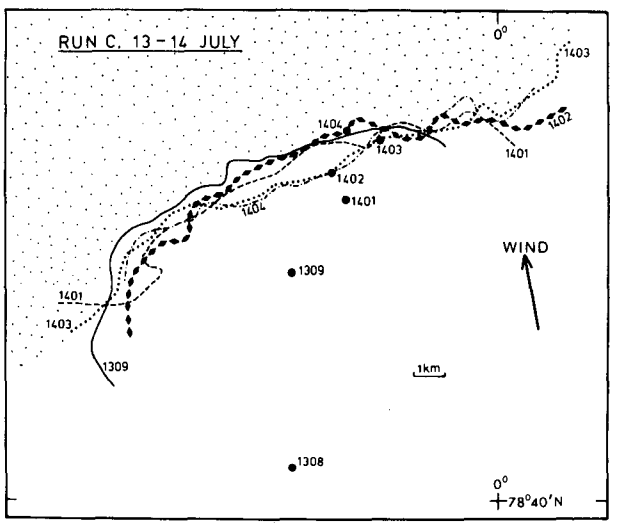

FIG. 3b. Wave station positions, run C (excluding 1307). Separate ice edge positions are shown for each of the stations.

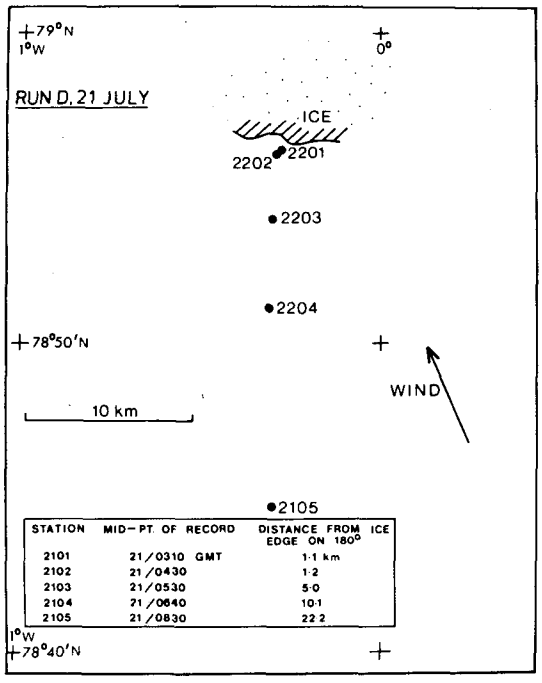

FIG. 4. As in Fig. 1 but for run D.

b. *Band experiments*

A first attempt at a band experiment was made on 10 July, with two IOS buoy stations on opposite sides of a narrow band which lay N–S just outside of the main ice edge. It was found, however, that the main sea direction came from the south with the waves being incident along the main axis of the band and reaching both sides of the band independently. The results are therefore not informative on the effect of the band on waves and will not be considered further.

A second and more successful band experiment (Fig. 5), carried out on 11 July, comprised three stations. A well-defined narrow band lay nearly parallel to the wind on a NE–SW bearing. The first station, 1101, was done from 0755–0835 GMT just to seaward of the band, using the IOS buoy. The ship then passed through the band and deployed the IOS buoy again at 1102, from 0855–0932 GMT. At this location both sides of the band were clearly visible on radar, so it was possible to map the band's width (Fig. 5), which varied from 230 m (about six rows of floes) at its narrowest to 1.3 km at its widest. Finally, a second open water station was done further from the band (1103, from 1010–1048 GMT). The wind remained relatively steady in speed and direction (216°/9 m s^{-1} at 1101; 194°/7.7 m s^{-1} at 1102; 213°/7.8 m s^{-1} at 1103). On its downwind side the band edge was sharp and well defined, but on its upwind side there were many loose cakes of rotting ice lying away from the band edge; this is typical of band behavior as observed by Martin et al. (1983). The ice within the band was composed of rotted wave-washed floes typically 40 m in diameter and 2–3 m thick.

4. Data analysis

a. *Evaluation of directional spectra*

The determination of the directional spectrum of the sea surface, whether from data collected by the IOS pitch–roll buoy in the open sea or from the SPRI heave–tilt sensor deployed on ice, follows the method first suggested in Longuet-Higgins et al. (1963) and Cartwright (1963). The technique has been used extensively by IOS (e.g., see Ewing and Pitt, 1982), but has not been applied to data collected on ice floes before. We summarize it in appendix A.

Both the pitch–roll buoy and heave–tilt sensor provide measured data at 0.5 s intervals. Each recording for the pitch–roll buoy is of 2048 s (34 min) length and, by use of the Fast Fourier Transform (FFT), we obtain estimates of the relevant cross-spectra by standard smoothing procedures to provide spectral estimates at 0.01 Hz interval with 40 degrees of freedom. Due to the shorter records obtained on the heave–tilt sensor and the fact that the spectra are composed of only long period waves (the short seas having been filtered out by the ice en route) less smoothing is demanded in order that the energy peak be resolved. Thus for heave alone the spectra are smoothed at 20 degrees of freedom. The cross-spectral computation is, however, the same as for the pitch–roll buoy. In both cases the wave height spectrum is obtained by dividing the acceleration spectrum by (frequency)^4 before smoothing.

b. *Determination of the reflected energy*

The statistical parameters θ_1 and θ_2 discussed in the previous section cannot give the detailed information

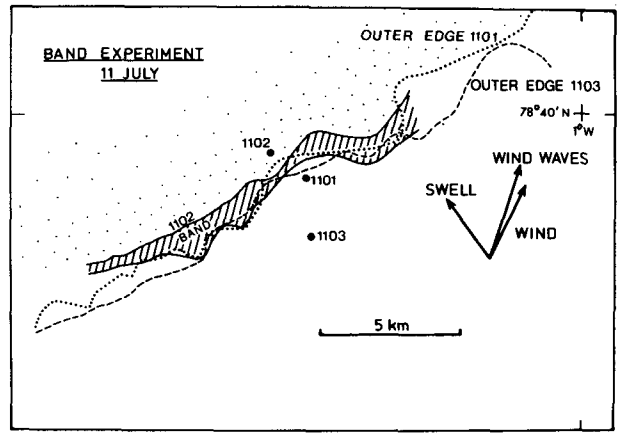

FIG. 5. The geometry of the band experiment of 11 July, showing the shape and orientation of the band relative to incident sea and swell, and the station positions.

on the directional distribution which is needed to detect the presence of reflected wave energy for pitch–roll buoy measurements made near the ice edge. A sophisticated new variational technique has been developed (Long and Hasselmann, 1979; Lawson and Long, 1983) which is capable of recovering bimodal directional distributions. In this method a function, called the "nastiness function," is minimized subject to a number of constraints. These constraints are that the directional spreading is non-negative and that the difference between the estimated directional spectrum and some favoured model is minimized. Random variability in the cross-spectral estimates is also taken into account. We now outline the basis of the variational method.

From section 4a we define a data vector $\mathbf{d} = (A_1, B_1, A_2, B_2)$ and a vector $\mathbf{b} = (\cos\theta, \sin\theta, \cos2\theta, \sin2\theta)$. Then

$$\mathbf{d} = \int_0^{2\pi} G\mathbf{b}d\theta, \tag{2}$$

is a set of four linearly independent data equations and G is the "true" spreading function which is required. Since observations of $\mathbf{d}$ contain random errors ϵ we write $\tilde{\mathbf{d}} = \mathbf{d} + \epsilon$. The inverse problem to be solved is then

$$\tilde{\mathbf{d}} = \epsilon + \int_0^{2\pi} G\mathbf{b}d\theta, \tag{3}$$

where G is to be determined.

Following the notation of Long (1985) we define the solution to Eq. (3) as that choice of $G = \hat{G}$ for which the "nastiness" function

$$\eta = \epsilon^T\mathbf{Q}\epsilon + \alpha \int_0^{2\pi} (\hat{G} - G_0)^2 d\theta = \min. \tag{4}$$

Here $\mathbf{Q}$ is a symmetric positive-definite matrix and G_0 is some favored distribution expressing our ideas about what the solution should look like.

Any known data-independent constraints on the solution may be incorporated into (4) using Lagrange multipliers. We insist that G be non-negative so that (4) becomes

$$\eta = \epsilon^T\mathbf{Q}\epsilon + \alpha \int_0^{2\pi} (\hat{G} - G_0)^2 d\theta + \beta \int_0^{2\pi} (\hat{G} - |\hat{G}|)^2 d\theta. \tag{5}$$

As explained in Long (1985) we may obtain exact fits to the inverse problem by setting $\alpha = 0$; most of the calculations in this paper are for this condition. For cases where α is nonzero we have made the calculations for a favored model of the form $G_0 \sim \cos^{2s}[(\theta - \theta_1)/2]$ where s and θ_1 are determined from A_1 and B_1.

Minimization of η is carried out subject to the condition that ϵ is consistent with a choice of 80% confidence level.

5. Results

a. Attenuation experiments

Results are discussed out of chronological sequence, in the order C, B, D, A, since this permits the implications of the experimental results to be developed logically.

1) RUN C, 13–14 JULY

Figure 6 shows energy spectra from the seven stations occupied during run C, for which the positions are shown in Fig. 3. Each spectrum shows a clear swell peak and wind-wave peak, and all are very similar in shape except for 1403, which shows a slight loss of energy at high frequencies (>0.3 Hz); 1307, which shows some energy loss at 0.15 to 0.2 Hz, a large loss at 0.2 to 0.35 Hz and a regeneration at the highest frequencies; and 1404, which shows a very large loss of energy at higher frequencies. We may ignore 1307, since it was the most remote station from the ice edge (Fig. 3a) besides taking place two hours earlier than any other station. The small but measurable attenuation at station 1403 relative to 1308–1402 is undoubtedly due to the few loose pieces of ice which lay between 1403 and open water. Their contribution cannot be assessed theoretically. Station 1404, however, is clearly an in-ice station, and we can assess the attenuation due to 1.2 km of ice by comparing 1404 with the mean of 1309, 1401 and 1402 which appear to be samples of an almost stationary and homogeneous sea.

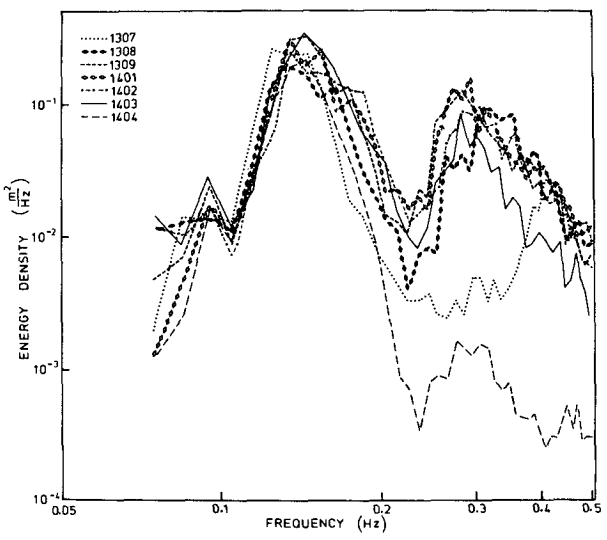

FIG. 6. One-dimensional energy spectra from the stations of run C.

Figure 7 shows the results of this computation. The ratio of the energy density at station 1404 (E_x) to the mean of the energy densities at stations 1309, 1401 and 1402 (E_0) is plotted against frequency. Apart from the very lowest frequencies, the main feature of the attenuation is a rapid decline in energy ratio from near unity at 0.15 Hz to about 10^{-2} at 0.25 Hz, followed by a modest recovery.

The theory with which we compare these results is the one-dimensional scattering theory of Wadhams (1973, 1975, 1978, 1986). In this theory the energy reflection coefficient $r_i(f)$ of a floe of diameter d_i and thickness h_i is calculated using linear potential theory to match velocity potentials in the open water and under the ice; the floe is allowed to heave and flex with a boundary condition of zero bending moment and shear at its ends. If floes of diameter d_i occupy a fraction p_i of the sea surface within the ice field, a wavefront penetrating into the ice will encounter, on average, (p_i/d_i) floes of this diameter per unit penetration, suffering a fractional loss of r_i at each encounter. This is equivalent to an exponential energy decay with distance, i.e.,

$$E_x = E_0 \exp(-\lambda_i x), \tag{6}$$

where

$$\lambda_i = (p_i/d_i) \ln(1 - r_i). \tag{7}$$

In an ice field of mixed floe sizes, the attenuation rate is computed by summation:

$$\lambda(f) = \sum_i [(p_i/d_i) \ln(1 - r_i)]. \tag{8}$$

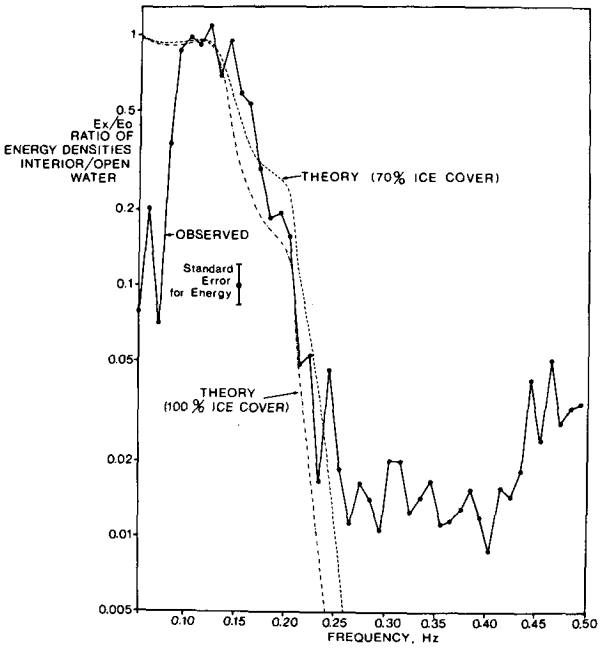

FIG. 7. The ratio of the energy density at station 1404 to the average energy density for 1309, 1401 and 1402. The theoretical curve is based on a one-dimensional scattering model with the floe sizes as given in Table 2.

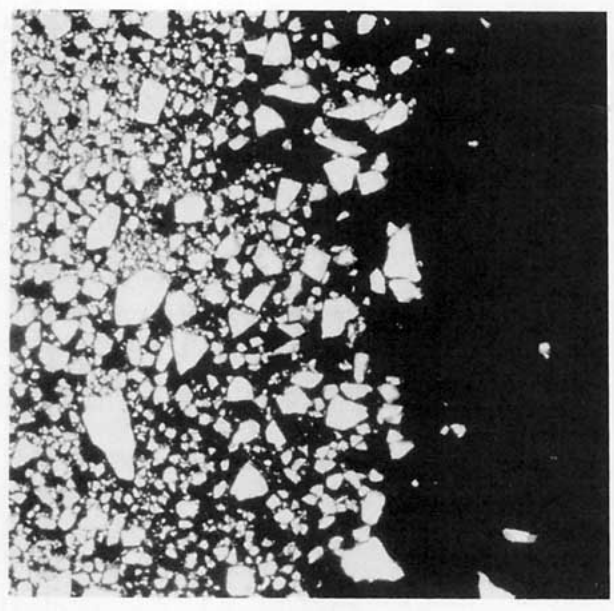

FIG. 8. An aerial photograph of the ice edge at approximately 80°34'N, 4°23'W on 28 June. The frame width is 305 m. (Photograph courtesy of A. M. Cowan.)

Wadhams (1973, 1986) showed that the $\lambda(f)$ of (8) should be further multiplied by a factor 2/3 to allow for multiple scattering, i.e., for wave vectors which have been reflected and which have suffered a secondary forward reflection.

The problem of obtaining suitable p_i, d_i and h_i values arises because aerial photography was not available from *Kvitbjørn*. Instead, we use as our data source the sum of six frames of 70 mm Vinten aerial photography data obtained by A. M. Cowan of SPRI during helicopter crossings of the ice edge from *Polarstern* in the same region a few days earlier (2–4 July). A typical frame is shown in Fig. 8.

Analysis of these frames yielded 228 floes which were binned in the size classes shown in Table 2 to yield equivalent values of p_i (l_i are fractional lengths used in a later computation). The boundaries of each bin lay half-way between the successive d_i values shown, and the p_i's are normalised to 100% total ice cover.

TABLE 2. Floe size data used in attenuation rate computation.

$d_{i,m}$	$h_{i,m}$	l_i	p_i
12.5	1.5	0.002	0.0001
15	1.5	0.004	0.0005
25	2	0.006	0.0010
35	2	0.030	0.0065
55	2	0.103	0.0376
80	2.5	0.087	0.0414
100	2.5	0.198	0.1256
150	3	0.293	0.2839
250	3	0.277	0.5035

The computation was carried out for x = 1200 m (Fig. 3), which assumes a 100% total cover, and for x = 840 m (a 70% total ice cover as per our visual estimates). The results are shown in Fig. 7. The fit of theory to data is excellent over a wide range of frequencies (0.10 to 0.26 Hz, i.e., about 4–10 s period), in fact the critical range where the attenuation is varying rapidly with frequency. At very low frequencies the theory predicts almost no attenuation, while the observations actually showed more energy inside the ice cover than outside. We suspect, from examining Fig. 6 and in the light of a similar phenomenon observed in run D, that this is a natural variation of the swell amplitude during the four hours of experiments. At high frequencies (>0.26 Hz) the theory predicts a very low energy ratio while the observed ratio appears to show some recovery. One possible explanation is wind-induced wave growth within the ice field, although we think this unlikely in view of the high ice concentration. A more likely possibility is a nonlinear transfer of energy from low to high frequencies, due to processes concerned with interactions between adjacent ice floes (collisions etc.) and their wave-making abilities. A linear theory cannot predict such a transfer of energy between frequencies, yet it is known to occur from observations of isolated floes brought into motion by seas. Events such as floe slamming, which presumably generates a broad spectrum of short period return waves, are believed to contribute to the observed increase in ratio above 0.25 Hz. A theoretical treatment cannot yet be given.

At frequencies below 0.08 Hz the small values of observed acceleration approach the noise level of the system and do not allow the wave height spectrum to be estimated reliably. Low values of the check ratio R confirm this conclusion. It is therefore likely that the deviation from theory at low frequencies is an instrumental effect.

We now examine the characteristics of the directional part of the spectrum using the variational technique to obtain information on the existence of the reflected wave energy near the ice edge. A number of computations were made for "exact fits" to the data ($\alpha = 0$) and with α allowed to vary so that the solution can move towards the favored model as far as the 80% confidence limits will allow. Figure 9 shows the results for the directional analysis at a frequency of 0.285 Hz for record 1401. With $\alpha = 0$ there is a secondary peak in a direction of 215°. Using the same data but with α allowed to vary and a favored model consisting of a unimodal distribution, we still obtain a secondary peak with about the same energy, although with a broader distribution. We believe that this analysis indicates that the secondary peaks are statistically significant.

Calculations for exact fits ($\alpha = 0$) were then made for the sequence of wave buoy records 1308–1403. Figure 10 shows the results for the analysis at a typical swell frequency (0.145 Hz) and a wind-wave frequency

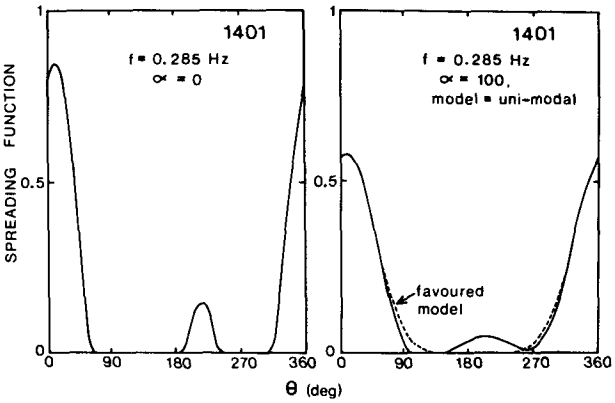

FIG. 9. Directional analysis of wave energy at a frequency of 0.285 Hz, station 1401, using two models.

of 0.295 Hz. The main swell peak was in a direction 320° while the wind sea was in a direction 020°. For both swell and wind waves we observe secondary peaks with the proportion of reflected wave energy increasing systematically as the ice edge is approached. Table 3 shows the proportion r of reflected wave energy at different distances from the ice edge. The broadening of the directional distribution is also confirmed by values of θ_2 which increase as the ice edge is approached for both wind sea and swell. (Standard deviation of θ_2 is ~4.0°; Long, 1980).

The wind-sea reflected energy is larger than that of the swell. This is expected on the basis of the scattering model, but the absolute values differ somewhat from theoretical predictions. A guess at the reflection coefficient based on the Wadhams' scattering model is that the reflected energy comes entirely from the front row of floes, and is therefore an average of the energy reflection coefficients r_i of the various floe sizes (d_i, h_i) present, weighted by the fractional length of the ice front occupied by each size rather than by the fractional *area* of ice field. Reanalysis of the aerial photographic data on this basis yields the revised set of fractional lengths l_i shown in Table 2. Application of the model then yields percentages of reflected energy as shown in Table 4. As Table 3 shows, while the reflected energies in the swell band approach those theoretically predicted, the energies in the wind-wave reflections are much lower. However, it is also clear from inspection of Table 3 that the observed percentage reflections increase as the ice edge is approached. This raises the question of open-water attenuation of the reflected energy, and thus at what distance the theoretical values of r are applicable. We discuss this question in section 6 with reference to the combined results of runs B, C and D.

Finally, we note from Table 3 how the main parameters of directionality (θ_1, θ_2) vary over the stations. The swell appears to show no evidence of refraction at the ice edge, as θ_1 at station 1404 within the ice is un-

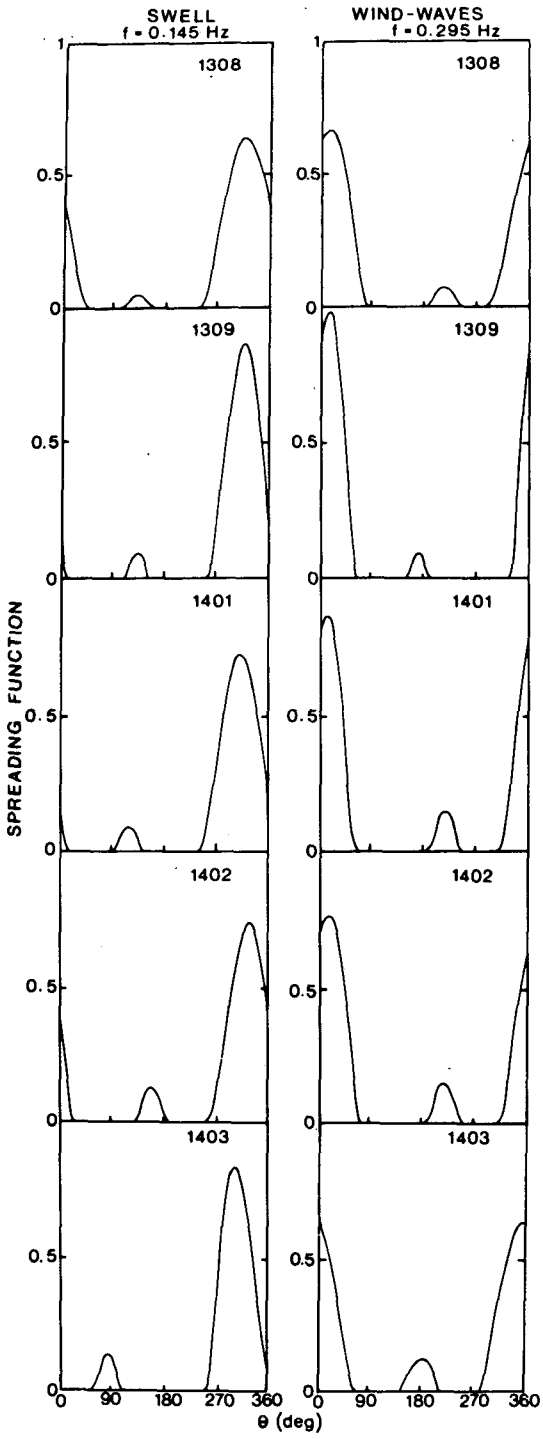

FIG. 10. Directional analysis of wave energies at the swell and wind-wave peaks of the spectra, assuming an $\alpha = 0$ model.

changed; also there is no evidence of a change of spread, with θ_2 being unchanged (± the standard deviation of 4.0°). The wind sea was steadily veering to the west as the stations progressed, but its main feature is a sudden onset of an almost isotropic sea with station 1404. The spread (71°) is so close to that of an isotropic spectrum that θ_1 is really undefined. Clearly, then, the effect of 1.2 km of ice is to broaden the spread of the wind-sea spectrum to an isotropic form while leaving the spread of the swell unchanged. This phenomenon is discussed further in section 6.

2) RUN B, 12–13 JULY

Figure 11 shows the one-dimensional wave spectra for records 1201, 1202, 1203 and 1301 collected within the pack ice, and records 1302–1306 collected in the open sea off the ice edge. In the open sea the spectra are made up of a swell peak and a wind-sea peak. The wind sea shows some variability as the experiment progresses, which is attributed at least in part to changes in both fetch and duration, as well as effects due to the progressively increasing distance from the ice edge. The onset of ice causes a large attenuation throughout the frequency range, which is greatest at high frequencies. However, the heave–tilt data are unreliable at the highest frequencies because of spurious energy introduced by the manual digitizing. We conservatively estimate that 0.2 Hz is the highest frequency at which we may safely interpret the data; the valid range is shown in Fig. 11. The real energy at high frequencies must be lower than that shown in the spectra, so that the high frequency attenuation caused by the ice is even more pronounced in reality.

If energies at 0.1 Hz, near the peak of the spectra, are plotted as a function of distance from the ice edge (with 1302 taken as representing the ice edge energy), it is found that a good fit to the exponential decay predicted by equation (1) is obtained (Fig. 12), with a λ of 3.4×10^{-4} m^{-1} adjusted to take account of wave direction. This value compares well with previous results from the same region (Wadhams, 1978). A theoretical computation using (8) and the data from Table 2 yields a prediction of 0.6×10^{-4} for λ, which is somewhat low but within the same magnitude. An accurate prediction for λ is crucially dependent on details of the floe size distribution, and the absence of site-specific data hampers a comparison in this case.

Table 5 shows the way in which the significant wave height h_s, calculated from the area under the spectrum, diminishes with penetration into the ice, and also shows that the total energy in the open water spectra increases slowly with increasing distance from the ice edge.

Table 5 also gives information about mean wave direction θ_1 and the directional spread θ_2 of the waves at the peak frequency f_m of each spectrum plotted in Fig. 11. For records 1302–4 the swell direction θ_1 was steady at about 290° corresponding to the most energetic part of the wave spectrum. The directional data obtained from stations 1201 and 1202 both have large angular spreads (60–80°), indicating that the wave field was isotropic in the area of measurement. Note that here even the long period swell has spread to become

TABLE 3. Significant wave height (h_s), position of spectral peak (f_m), mean wave direction (θ_1) and directional spread (θ_2) for the swell portion (0.055–0.215 Hz) and the wind-wave portion (0.255–0.495 Hz) of the spectra from run C. The table also shows the percentage of reflected energy at the spectral peak, computed using the Long-Hasselmann method.

Record no	Distance off ice (km)	Swell (0.055–0.215 Hz)					Wind sea (0.255–0.495 Hz)				
		h_s (m)	f_m (Hz)	θ_1°	θ_2°	r (%)	h_s (m)	f_m (Hz)	θ_1°	θ_2°	r (%)
1307	19.9	0.43	0.145	310	28	—	0.19	0.415	037	24	—
1308	9.1	0.41	0.135	321	34	2.6	0.39	0.315	002	23	4.1
1309	4.2	0.48	0.145	319	30	3.5	0.40	0.285	017	28	3.4
1401	1.8	0.48	0.135	321	31	3.7	0.43	0.295	012	31	5.5
1402	1.2	0.45	0.155	317	37	5.5	0.40	0.305	007	35	8.0
1403	0	0.50	0.145	311	29	5.4	0.30	0.285	347	36	8.8
1404	−1.2	0.36	0.145	311	32	—	0.017	0.305		undefined	

isotropic, but the distances into the ice at which the measurements were made (17.8 and 22.5 km) were very much greater than in run C. This suggests that the swell increases its directional spread more slowly than the wind sea, an effect discussed further in section 6.

A useful way of presenting this type of data graphically is in the form of energy density plotted against frequency and wave direction. We have contoured the results from the heave–tilt station 1301 and the IOS pitch–roll station 1302 with contour levels as shown in Fig. 13. This demonstrates clearly the way in which a relatively narrow spectrum measured off the ice is transformed into an almost isotropic distribution in the interior of the ice.

Reflected energy percentages are also shown in Table 5, computed using the Long-Hasselmann method with $\alpha = 0$. Assuming that floe size distributions were similar to run C, we can see by comparison with Table 4 that the observed reflections fall within the lower part of the range of theoretical predictions.

3) RUN D, 21 JULY

Figure 14 shows energy spectra from the five stations occupied during this experiment (for map of positions, see Fig. 4). There is no important change in the shape of the energy spectra during the experiment. The spectra are simple in form; at the high frequency end the energies approach the curve for the saturation range of a wind-generated sea, given by Phillips (1980) as

$$E = \gamma g^2 \omega^{-5}, \tag{9}$$

where $\gamma = 1.23 \times 10^{-2}$ and $\omega = 2\pi f$, the angular frequency. However, the peak of the spectrum, at about 0.13 Hz, is characteristic of a sea generated by a wind of 15–19 m s^{-1} while the observed wind speed was 4 m s^{-1} during and before the experiment. Thus these spectra represent a swell from a distant generating area.

Differences between the energies are not significant over most of the spectral range. The 80% confidence interval for energy density, calculated from a χ^2 distribution on the basis of 40 degrees of freedom (Bendat and Piersol, 1971), is shown in Fig. 14 ($0.77\hat{E} < E < 1.38\hat{E}$). With five spectra, this interval can be expected to approximate to the range of observed energy densities at each frequency, and in fact does so except at the spectral peak, where growth appears to be occurring. This effect is shown in Table 6, which also shows the mean wave direction θ_1 and directional spread θ_2 at the spectral peak.

The significant wave height h_s computed over the frequency range (0.055 to 0.355 Hz) varies from 0.63 m at the first station to 0.90 m at the last. For a Pierson-Moskowitz spectrum, Cavanié (1980) showed that the relative standard error $\sigma(h_s)$ in the significant wave height is given by

$$\sigma(h_s) = 0.57/\sqrt{n} \tag{10}$$

where n is the number of degrees of freedom. With $n = 40$, $\sigma(h_s) = 0.09$ and the difference between h_s at 2101 and 2105 is significant at better than the 0.1% level. There is thus significant wave growth occurring during the 5-hour duration of the experiment, especially at the spectral peak, but such variations in swell intensity lie well within normally observed limits.

We now examine the directional part of the spectra. As Table 6 shows, the mean direction of the swell peak θ_1 remains relatively steady throughout the stations, but its directional spread θ_2 increases near the ice edge. This increase, although not great, is significant since the standard deviation for θ_2 is 3.8°. The increased spread is a symptom of the presence of reflected wave energy, and Table 6 also shows the results of a Long-

TABLE 4. Theoretical reflection coefficients of energy from the ice edge.

Swell band		Wind-wave band	
Frequency (Hz)	r	Frequency (Hz)	r
0.135	6%	0.285	83%
0.145	12%	0.295	85%
0.155	18%	0.305	85%
		0.315	82%

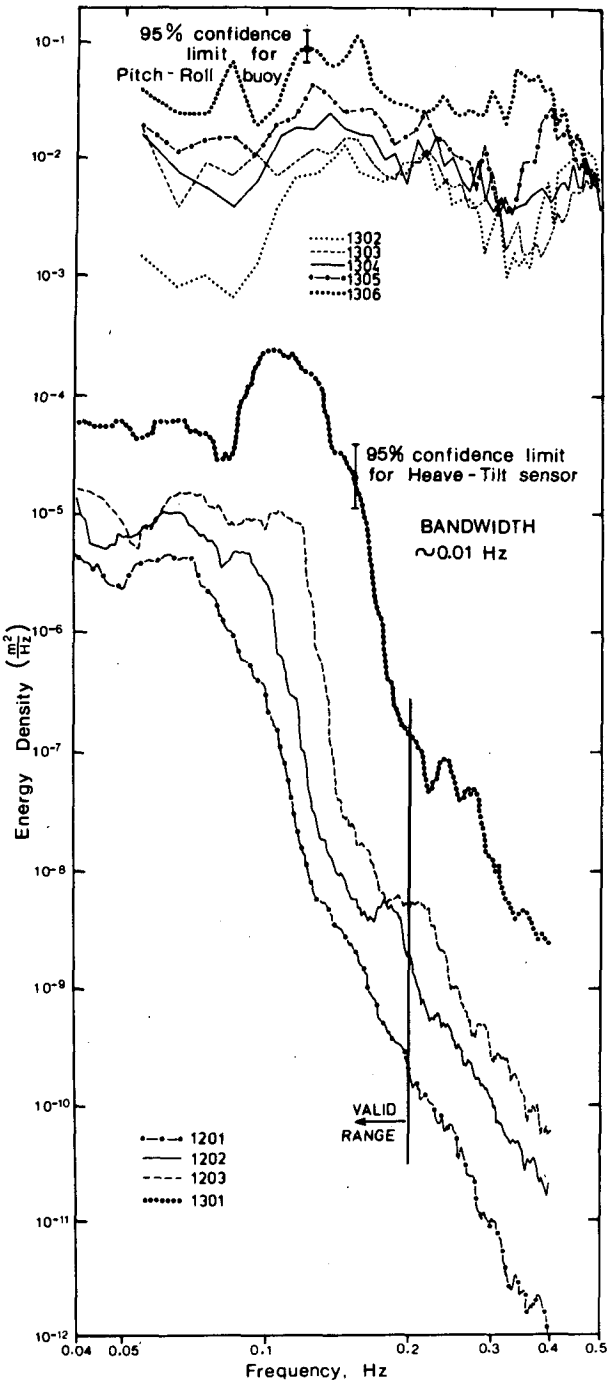

FIG. 11. As in Fig. 6 but from run B.

Hasselmann analysis ($\alpha = 0$) of the reflected wave energy percentage at the spectral peak. Near the ice edge the reflected energy percentages are high and agree well with the predictions of scattering theory at these frequencies (Table 4). The reflected percentage decreases with increasing distance from the ice edge, as also observed in runs C and B. We discuss this effect in section 6.

4) RUN A, 8–9 JULY

Various problems were encountered with instrumentation during run A, which chronologically was the first experiment to be carried out. These resulted in a limited pitch–roll buoy dataset, which comprises data at sites 0902, 0903 and 0904, and heave–tilt sensor datasets for stations 0904 and 0905 (see Fig. 1). Fully directional measurements are only available at sites 0903–0905 since the amplitude of the seas were such that the pitch–roll buoy tiltmeters were initially incorrectly set.

Energy spectra for stations 0902–0905 are shown in Fig. 15. At 0902, located some 6.3 km from the ice edge, the spectrum has both a swell peak at 0.10 Hz and a wind-sea peak at 0.44 Hz. The significant wave height h_s in this case is 0.34 m. By the time the ice edge is reached (at 0903), the wind-sea maximum in the spectrum has vanished but the swell peak still remains at 0.1 Hz and similar amplitude. The significant wave height is now 0.22 m. Station 0904 is located approximately 4.1 km within the pack ice. At this site two records were obtained; the first from the pitch–roll buoy in the water, the second from the heave–tilt sensor located on a large ice floe. Examining the energy spectrum from the buoy relative to the open water spectra, we see the usual frequency-dependent energy decay observed in our other datasets with most attenuation taking place at wind-sea frequencies and little at swell frequencies. There is a discrepancy between this spectrum and that computed for the heave–tilt sensor located on a nearby ice floe. This can be attributed to the seakeeping characteristics of the ice floe, which was very large (~250 m) in comparison to all the wavelengths at which significant energy existed in the incident sea (the wavelength corresponding to the swell's peak was ~150 m). The heave response of the floe may be found in the work of Squire (1983) who presents the gain factor for the vertical motion on the floe in relation to the incident wave's amplitude as a function of nondimensional wavelength (defined as wavelength/half-diameter). From Fig. 3 of Squire (1983) we see that a small value of nondimensional wavelength implies a small value of gain factor, implying imperfect coupling between ocean and ice. Near perfect response for a floe of this size is not achieved until waves of period ~20 s force the floe, far beyond the periods seen in the incident seas during this experiment. Station 0905, also a heave–tilt measurement on a large floe, shows extremely similar characteristics to 0904, but with slightly less energy. As can be seen from Fig. 15, the spectra for 0904 and 0905 are very similar in form.

Figure 16, plotted as a function of frequency, shows the ratio of energy density between the pitch–roll station at 4.1 km penetration (0904) and that just outside the ice edge (0903). The theoretical curve derived from the one-dimensional scattering theory, and based on the empirical distribution of floe sizes and thicknesses reported earlier (Table 2), using $x = 5700$ m as an

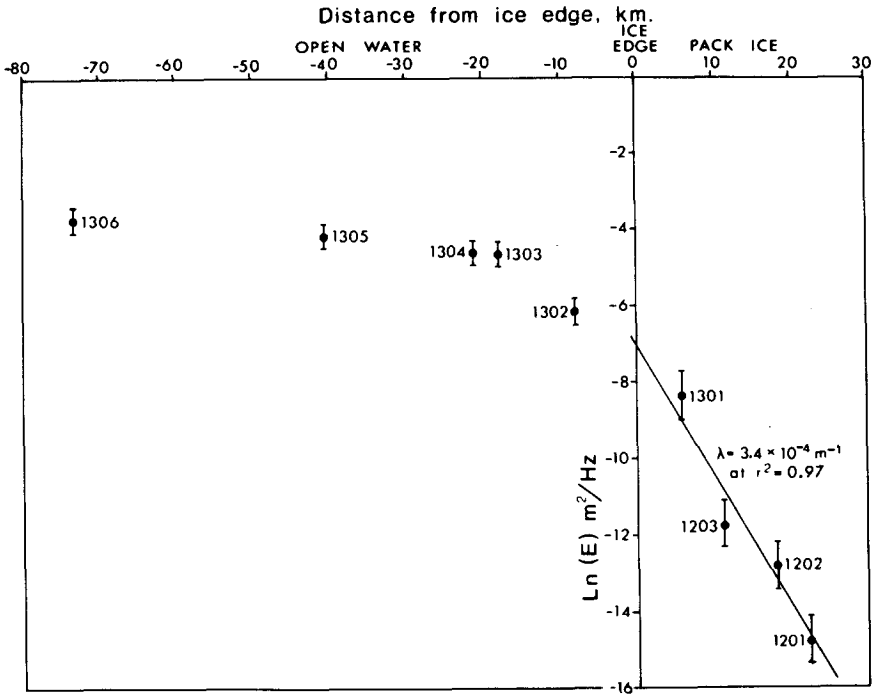

FIG. 12. Wave attenuation in the ice at 0.1 Hz.

appropriate penetration based on the swell direction, is also plotted. The data fit the theory reasonably well over the range of periods (~5.5–13 s) where attenuation varies rapidly with frequency. At high frequencies (>0.2 Hz) the theory predicts low attenuation while the data show a leveling-off of the energy ratio. Again this is probably due to short period waves being induced by the motion, and hence wave-making capability, of ice floes adjacent to the wavebuoy.

The directional characteristics of the wave spectra inside and outside the ice margin confirm our earlier conclusions. Unfortunately, we have only one station off the ice edge (0903) which may be interpreted for directionality. This dataset gives a principal swell direction θ_1 of ~335° and a spread θ_2 of ~35°. The spectrum is isotropic over wind-sea frequencies, though as noted earlier the energy density is also very small here. Both the pitch–roll and heave–tilt stations at 0904 show the wave field to be isotropic over the entire range of frequencies present in the incoming sea. The same is true at station 0905 further into the ice cover.

b. *Band experiment, 11 July*

When analyzing the results of the band experiment, it was found that a fault had developed in the pitch–roll buoy during station 1103, so that its data are invalid. We therefore consider only stations 1101 and 1102. Figure 17a shows energy spectra of heave from

TABLE 5. The significant wave height (h_s), frequency of maximum energy (f_m), mean wave direction (θ_1), directional spread (θ_2), and reflected energy for records 1201 through 1306.

Record	Distance from ice edge (km)	h_s	Peak frequency (Hz)	θ_1°	θ_2°	% reflected energy at f_m
1201	−22.5	1.4 mm	0.064	undefined	76	undefined
1202	−17.8	2.3 mm	0.066	undefined	67	undefined
1203	−11.2	3.5 mm	0.070	.....	no data	.....
1301	−5.6	12.9 mm	0.104	.....	no data	.....
1302	8.2	0.15 m	0.145	285	42	12.7
1303	18.0	0.18 m	0.145	292	36	4.9
1304	21.1	0.22 m	0.135	299	37	6.1
1305	40.3	0.28 m	0.125	332	40	10.7
1306	73.0	0.46 m	0.155	344	37	4.7

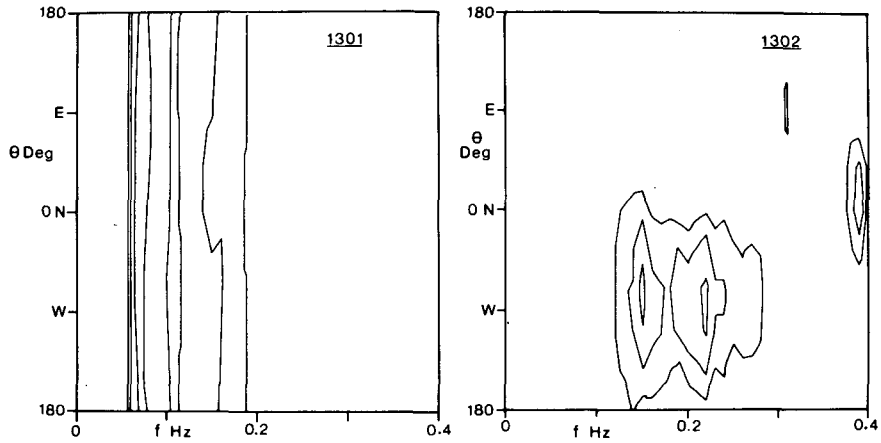

FIG. 13. Contours of the directional spectrum $F(f, \theta)$ for records 1301 and 1302. The base level for 1301 is 0.00000125 m^2 Hz^{-1} rad^{-1}, and for 1302 is 0.00125 m^2 Hz^{-1} rad^{-1}. The energy (contour spacing) increases by a factor 10 and by a factor 2 respectively. Upper level contour for 1301 is at 0.00125 m^2 Hz^{-1} rad^{-1}, and for 1302 is at 0.005 m^2 Hz^{-1} rad^{-1}.

these two stations. It is clear from inspection that the ice in the band has caused relatively little attenuation to the swell, but much greater attenuation of the shorter period waves. At the shortest periods of all (0.33 Hz upwards, i.e., less that 3 s period) the attenuation is again reduced, suggesting wave regrowth on the leeward side of the band.

Figure 17b, c show respectively the mean wave direction θ_1 and the directional spread θ_2 for the two stations. The wind waves had a predominant direction of about 018°, roughly parallel with the wind, while the swell waves were traveling towards 324° and were thus incident almost normally on the band. There is a quite sudden transition between the two wave trains, occurring at 0.25–0.30 Hz. After passage through the band, the swell direction remains almost unchanged, while the wind wave directions are ill-defined and show high variability. The directional spread parameter θ_2 for 1102 is narrowed for the swell regime while the wind sea values of θ_2 indicate a very broad and almost isotropic spectrum. A reasonable explanation is that the swell in 1102, having been relatively unaffected by the ice, consists largely of the original forward-going wave vectors, and so will remain narrow with a possible further narrowing due to the hypothesis of longer path lengths at slant incidence. The wind sea, however, has been heavily attenuated, and we expect that what emerges from the lee side of the band consists of wave vectors that have suffered multiple scattering and are therefore much less well collimated. We discuss this effect further in section 6.

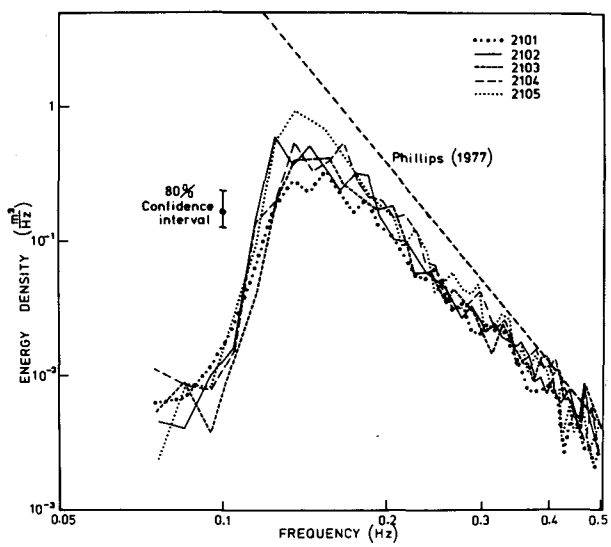

FIG. 14. Energy spectra from the wave stations in run D.

The ratios of leeward to windward energy densities were computed and plotted at 0.01 Hz intervals in Fig. 18. They were then compared with the results of the one-dimensional scattering theory. In this case an empirical distribution of floe sizes was used, based on visual observations and photographs taken as the ship traversed the band (Table 7).

The effective diameter of the band (x for Eq. 6) is different for different frequencies since the spectrum consists of two wave systems with differing directions. The radar image of the band (Fig. 5) was measured for width at equal intervals along its length for the bearings corresponding to wind sea and swell, giving (0.67 ± 0.06) km as the effective width for the swell and (0.90 ± 0.11) km as the effective width for the wind waves. These figures were used in the computation of E_x/E_0.

As Fig. 18 shows, the simple scattering theory gives a remarkably good fit to the observations throughout the frequency range up to 0.32 Hz, i.e., throughout the swell and longer wind–wave periods. The theory even

TABLE 6. The significant wave height (h_s), frequency of maximum energy (f_m), mean wave direction (θ_1), directional spread (θ_2), and reflected energy for run D.

Record	Distance from ice edge (km)	h_s (m)	Peak frequency (Hz)	θ_1°	θ_2°	% reflected energy at f_m
2101	1.1	0.63	0.155	318	33	8.3
2102	1.2	0.76	0.125	318	26	10.0
2103	5.0	0.72	0.145	316	29	5.4
2104	10.1	0.78	0.135	304	28	5.1
2105	22.2	0.90	0.135	304	22	3.5

reproduces the flattening of the energy ratio curve in the range 0.18 to 0.27 Hz. At frequencies higher than 0.32 Hz, the theoretical energy ratio continues to decline steeply with increasing frequency, while the observed ratio climbs back up towards unity. At such high frequencies, it is reasonable to ascribe this effect to local wind–wave generation in the stretch of open water lying between the band and the main ice edge.

The effect of the band on both the wave energy and the directional spread can again be seen graphically on a contour plot of energy density against frequency and wave direction. Figure 19 shows how the energy in the wind sea is dramatically reduced (to below the base level contour) by the presence of the band, while the remaining energy in the swell has a narrower spread.

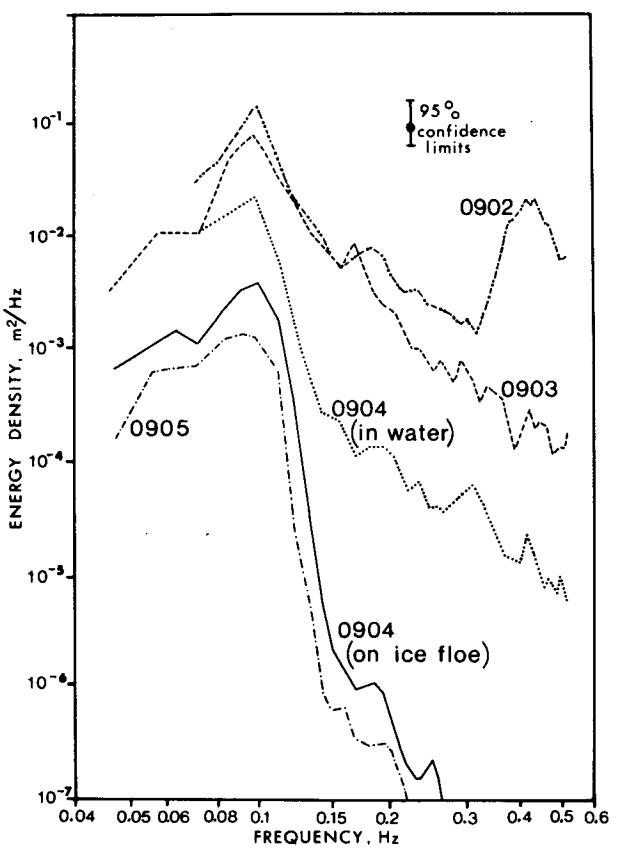

FIG. 15. As in Fig. 14 but from the wave stations of run A.

The amount of reflected energy in the spectra was computed using the Long-Hasselmann technique, and Fig. 20 shows the results for the swell peak at 0.155 Hz. Both spectra show some reflected energy, with estimated percentages of 3.8 for station 1101 outside the band, and 6.5 for station 1102 inside. Reflected energy at station 1101 can be expected to be due to the band, but the reflected component at 1102 is presumably due to reflections from the main ice edge lying further to the west. The scattering model, using data relevant to the floe size distribution in the band (data of Table 7 modified to a set of l_i values appropriate to line densities), predicts a reflection coefficient of 9.4% at this frequency, while the distribution in Table 2, which may be more relevant to the main ice edge, predicts 17.8%. Both these values are greater than the observed reflections, but it is noteworthy that the predicted reflection from the floes in the band is lower than the predicted reflection from the generally larger floes in the main ice edge, which corresponds to the sense of the observed results.

It is of interest to studies of band dynamics to estimate the wave radiation pressure exerted by the incident sea upon the band. Longuet-Higgins (1977) showed that the wave radiation pressure (force per unit width of wavefront) F_r exerted by a wave of amplitude a on a floating object from which it is reflected with

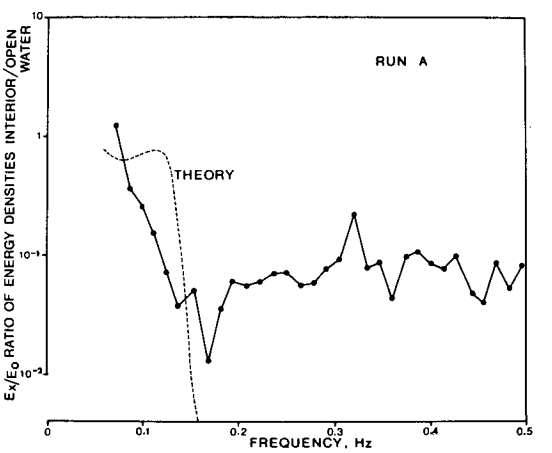

FIG. 16. Comparison of theory and data for the ratio of energy densities outside (0.7 km) and inside (5.7 km) of the ice edge. The comparison fails above 0.2 Hz where fetch limited wave may be occurring, or due to the wave-making oscillations of nearby ice floes.

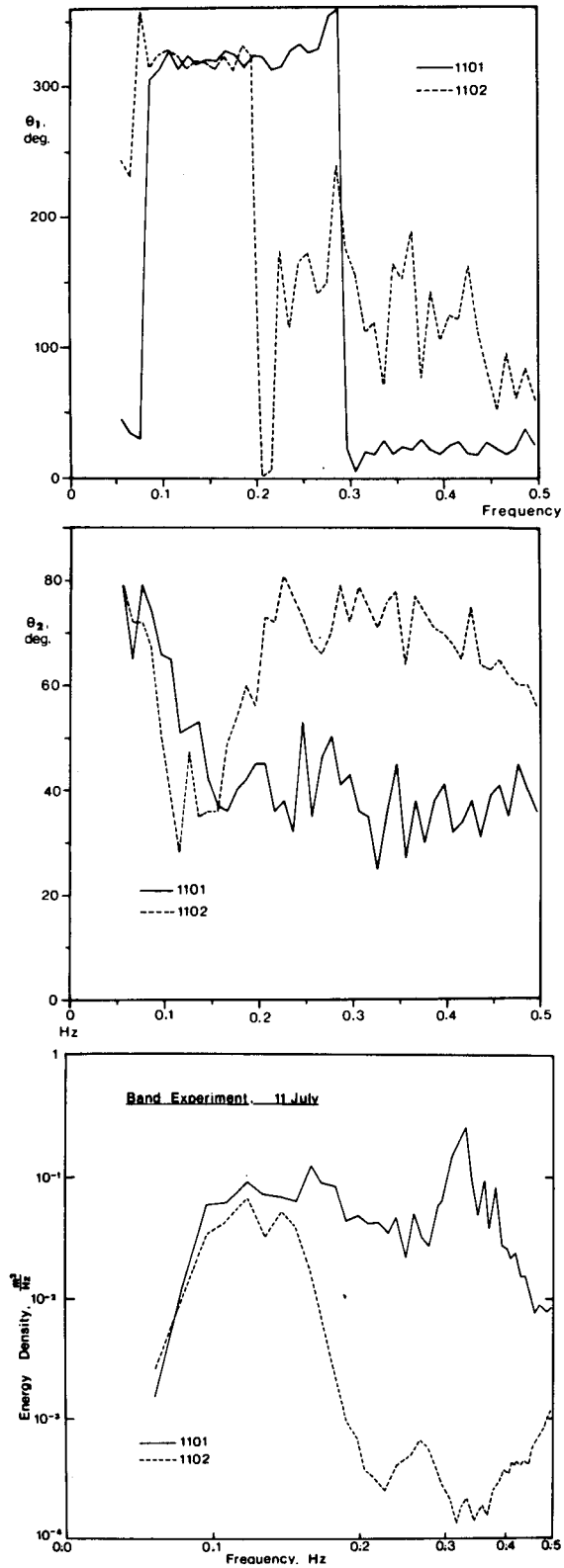

FIG. 17. (a) The two valid energy spectra and their corresponding (b) mean wave directions and (c) angular spreads for station 1101 upwind of the band and station 1102 downwind of the band. Note the decrease in wind sea across the band, with little or no change to the swell. Also note the sudden increase in spread for the wind sea after the band has been crossed.

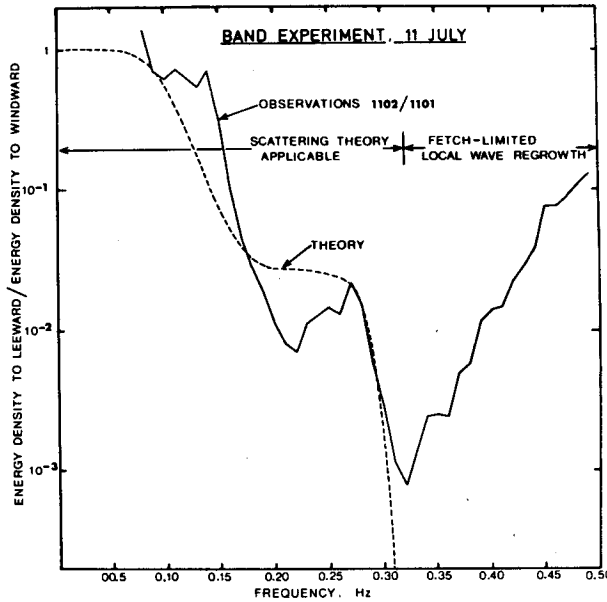

FIG. 18. Comparison of theory and data for the ratio of energy densities on both sides of the band. The comparison fails where fetch limited wave regrowth occurs above approximately 0.3 Hz.

amplitude a' and transmitted with amplitude b, is given by

$$F_r = \frac{1}{4}\rho_w g(a^2 + a'^2 - b^2). \tag{11}$$

In terms of energy reflection coefficient r, this becomes

$$F_r = \frac{1}{2}\rho_w g a^2 r. \tag{12}$$

We approximate a by $h_s/2$, half the significant wave height, and r by the reflection coefficient at the swell peak (in this way we do not consider the frequency dependence of the reflection). For the spectrum of 1101, this yields 19 N m^{-1} as the wave radiation pressure on the band. By comparison, using the observed wind speed of 7.7 m s^{-1} and MIZEX-84 drag coefficients of 1.8–4.0 $\times$ 10^{-3} (Guest and Davidson, 1984), we can estimate the direct wind drag on the band per unit length (i.e., integrated over the 670 m width of the band) to be in the range 70–155 N m^{-1}. Thus the direct wind forces driving the band at this time were about four to eight times as large as the wave forces.

TABLE 7. Floe size distribution in band, used for theoretical computation.

l_i	p_i	d_i (m)	h_i (m)
0.452	0.2	12.5	2.0
0.226	0.3	25	2.0
0.162	0.3	35	2.0
0.103	0.1	55	2.0
0.057	0.1	100	2.0

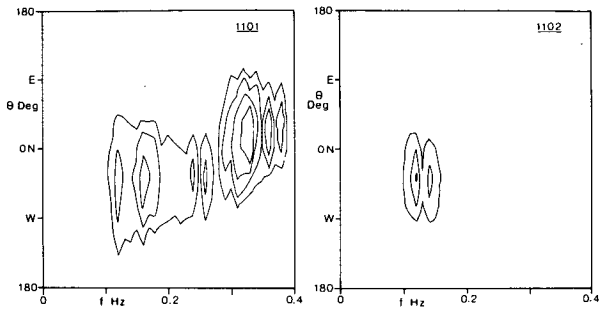

FIG. 19. Contours of the directional spectrum $F(f, \theta)$ for records 1101 and 1102. The base level in each case is 0.00125 m^2 Hz^{-1} rad^{-1}, the contour spacing is a factor of 2, and the upper level contours are at 0.10 m^2 Hz^{-1} rad^{-1} for 1101 and 0.05 m^2 Hz^{-1} rad^{-1} for 1102.

6. Discussion

We make the following general comments about our observations and the accompanying theory in relation to attenuation and changes in spectral directionality due to pack ice in the MIZ.

Attenuation. A full interpretation of the attenuation results observed in the various experiments reported in this study in relation to the one-dimensional scattering theory is hindered by the limited data available to interpret prevailing ice conditions (viz. floe size distribution and thickness). Despite this, in most cases visual observations recorded from the bridge of *Kvitbjørn* and aerial photography collected in the region enable several useful conclusions to be drawn from the data with respect to the energy decay offered by pack ice to penetrating ocean waves. We summarize these as follows:

- Pack ice in the marginal ice zone attenuates waves differentially; short waves are damped more than long waves. This has been observed in earlier experiments.
- A one-dimensional scattering theory predicts the energy decay well for frequencies up to approximately 0.25 Hz, but offers more attenuation at high frequencies and less attenuation at very low frequencies than is observed in the data.
- The disagreement between theory and data at low frequencies may be due to variation in swell amplitude over the duration of the experiment. Alternatively, since the accelerations are very small for long swells, the discrepancy may be due to instrumental imprecision.
- The disagreement between theory and data at high frequencies is due to either wind-induced wave regrowth or to waves generated within the ice from the wave-making motions of ice floes. The latter effect is most likely within the marginal ice zone proper, since it is known that ice floes can experience resonance if their dimensions tune to the incoming wave field, and floe–floe interactions such as collisions, rafting events, breaking waves, and the like, are common near the ice margin. Nonlinear transfer of energy between frequencies is also a possibility. Fetch limited regrowth is unlikely within high concentrations of pack ice (e.g., Fig. 7), but is a strong candidate to explain the increase in energy ratio shown in Fig. 18 for the band experiment.
- Direct comparison between pitch–roll buoy data and heave–tilt data presents some problems due to the fact that the buoy is in the water and the latter sensor sits on the ice. Thus the seakeeping characteristics of the ice floes enter the interpretation. In most cases this did not prove a difficulty since the floes were of moderate size. However, in Fig. 15, where the attenuation between stations is clear, no direct comparison between buoy and ice-sites may be made due to the large size of the floe.

Spread. An important and unexpected result of these experiments is the discovery that:

- The directional spectrum inside the ice field widens until it is essentially isotropic. For wind seas this widening happens within a very short distance; in run C the energy at 0.305 Hz has become isotropic within 1.2 km of the edge, in run A it is isotropic at 4.1 km, and in the band experiment it has become isotropic after crossing only 670 m of band. For the swell the process is slower; in run B the swell spread is isotropic at 17.8 km into the ice, in run A it is isotropic by 4.1 km, but in run C it shows no significant spread after 1.2 km, and in the band experiment it is actually narrower after 900 m of passage through the band. The picture then is of a swell (7+ s period), which initially narrows and then spreads after about 1–4 km of penetration into the ice, and of a wind sea (3–4 s period), which spreads to isotropy almost immediately and certainly in less than a km.

The probable explanation, although this requires further theoretical analysis, is that two competing pro-

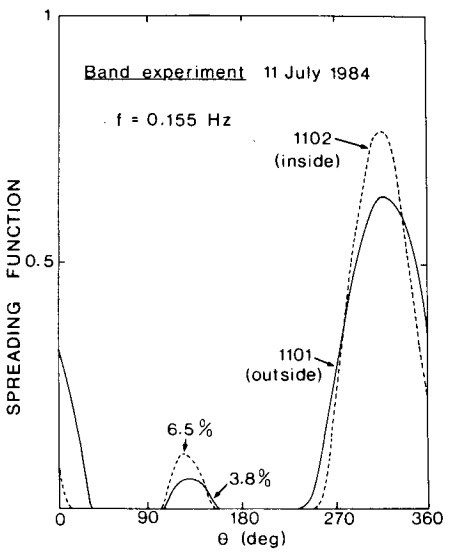

FIG. 20. Directional analysis of wave energy for stations 1101 and 1102 at 0.155 Hz.

cesses are at work. The narrowing occurs because of the path length effect mentioned in section 1, where waves incident at an angle θ to the normal must travel a distance ($x \sec\theta$) to attain a penetration x, and so are attenuated more than waves incident normally. The widening is intelligible if we consider the fate of the wave components which are scattered from the forward-going wavefront as it attenuates. If the attenuation rate is high (as in the case of high frequency wind waves) a site within the ice field will be bathed in scattered radiation from surrounding floes while at the same time the primary forward-going wave vector is progressively weakened by attenuation. Thus as x increases, the total wave energy decreases while at the same time becoming randomized in direction. A simple picture of this effect can be obtained by considering an incident directional spectrum with its peak at normal incidence and of a standard shape i.e.,

$$E(\theta, 0) = E(0, 0) \cos^{2n}\theta. \quad (13)$$

At a penetration x, the energy density will be of the form

$$E(\theta, x) = E(0, x) \cos^{2n}\theta \exp[-\lambda x(\sec\theta - 1)] + f_1(\lambda) f_2[E(\theta, x)] \quad (14)$$

where f_1, f_2 are increasing functions of λ and E (or of $|dE/dx|$) and account for the input of locally scattered radiation at random angles. The directional spread due to the first term alone in (14) will always be less than the initial spread (13), but the terms f_1, f_2, if large, will more than offset the narrowing.

Reflection. The following important conclusions are evident:

• Using the Long-Hasselmann method we have been able to find a significant reflected component in all of the spectra that were measured outside the ice edge. The measured energy reflection coefficient is of the order of a few percent (overall range 2.6–12.7). The simplest way of modeling reflection using the scattering model is to assume that the reflected energy seen outside the ice edge consists of backscattered energy from the first row of floes encountered by the incident wavefront. Typical distributions of floe diameters were used in running the scattering model; the modeled reflection coefficients are usually larger than those measured. The discrepancy is least for swell frequencies, where the modeling predicts reflection coefficients of 6–18%, and greatest at wind–wave frequencies, where the modeling predicts 82–85% reflection.

• In considering the reason for this discrepancy, we note that the measured reflection coefficient is a strong function of the distance from the ice front at which the measurement was made. Figure 21 shows energy reflection coefficient as a function of distance for all runs in which a number of open water stations were done. Each run shows a negative correlation between reflected energy and distance. The product-moment correlation coefficients are as follows:

Run C swell	Coefficient 0.87	Significance level 5%
wind waves	0.76	N/S
Run B swell	0.43	N/S
Run D swell	0.85	6%

The decline of measured reflected energy with distance is only significant in two cases. However, this does suggest that the reflected energies near the ice edge are real rather than being some background noise level generated by the Long-Hasselmann technique. Secondly it suggests that reflected components are lost from the spectrum within relatively short distances from the ice edge, 10–20 km being sufficient to dispose of at least half the energy. These distances are much less than the attenuation lengths of similar waves in the open sea, suggesting that backscattered radiation is attenuated rapidly in propagating through a wave field with the same frequency, greater energy and op-

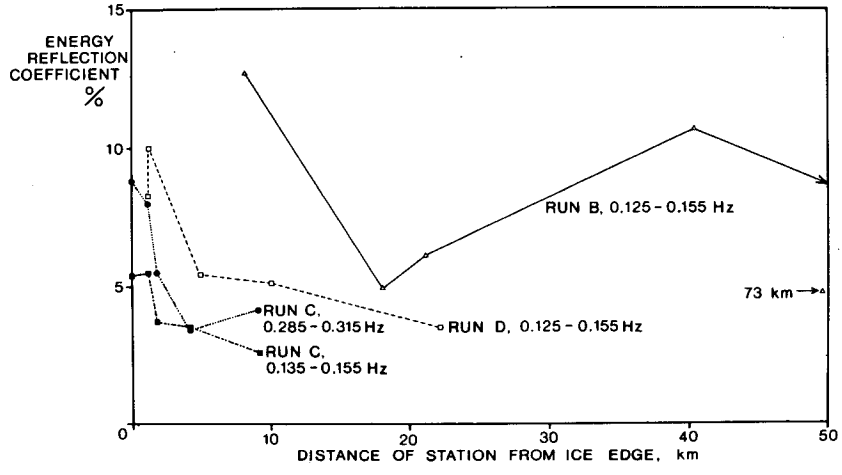

FIG. 21. Reflection coefficients versus distance from ice edge.

posite direction. There is an analogy here with reflections from cliffs and harbor walls, where a significant standing wave field is seen only very close to the wall. The implication is that the modeled reflection coefficients may not be erroneously large, but rather that this high reflection is only detectable very close to the ice front.

• A further significant result of the Long-Hasselmann analysis is that in all of the analyses the reflected spectral peak lies very close to 180° from the incident peak (Figs. 9, 10, and 20), despite the fact that the wave trains were not necessarily incident normally on the ice front. This supports the idea that reflection at the ice edge really is a backscattering rather than being a specular reflection.

Refraction. A negative but important result:

• In cases where the directional spectrum inside the ice has been measured before it becomes isotropic (run C, swell frequencies; band experiment) there is no evidence of refraction across the ice edge. If refraction does occur it is more likely that evidence for it will be found in remote sensing imagery, particularly synthetic aperture radar images which can display the structure of long-crested swell waves.

Acknowledgments. PW and VAS thank the U.S. Office of Naval Research, the Natural Environment Research Council of Great Britain, and the British Petroleum Co. Ltd. for financial support. Dr. R. B. Long kindly made available his computer programs for the calculation of directional spectra using the variational method. We also thank our colleagues Mr. S. C. Moore, Mr. K. Birch, Dr. C. H. Clayson, Ms. Ruth Weintraub and Mr. Robert Massom.

APPENDIX A

Calculation of Directional Parameters using the Classical Approach

The pitch, roll and compass channels are used to derive the two components of surface slope with respect to North–East axes. Let subscripts 2 and 3 denote the components of surface slope in the north and east directions respectively and let subscript 1 refer to the series for vertical acceleration in units of "g." Then it can be shown that the six cross-spectra derived from the wave buoy system are given by

$$C_{11}(f) = \int_0^{2\pi} (2\pi f)^4 F(f, \theta) d\theta,$$

$$C_{22}(f) = \int_0^{2\pi} k^2 \cos^2\theta F(f, \theta) d\theta,$$

$$C_{33}(f) = \int_0^{2\pi} k^2 \sin^2\theta F(f, \theta) d\theta,$$

$$Q_{12}(f) = \int_0^{2\pi} k(2\pi f)^2 \cos\theta F(f, \theta) d\theta,$$

$$Q_{13}(f) = \int_0^{2\pi} k(2\pi f)^2 \sin\theta F(f, \theta) d\theta,$$

$$C_{23}(f) = \int_0^{2\pi} k^2 \sin\theta \cos\theta F(f, \theta) d\theta, \qquad \text{(A1)}$$

where C_{ij} and Q_{ij} are the co- and quadrature spectra of series i with j; $F(f, \theta)$ is the directional wave spectrum with respect to frequency f and direction of propagation θ; k is the wave number. Only five of the cross-spectra are independent. This allows estimation of the five Fourier coefficients in the expansion of $F(f, \theta)$, namely,

$$a_n + ib_n = \frac{1}{\pi} \int_0^{2\pi} e^{in\theta} F(f, \theta) d\theta, \quad n = 0, 1, 2. \qquad \text{(A2)}$$

In the calculations, it is convenient to compute the normalized angular harmonics $A_1 = a_1/a_0$ etc., where a_0 is the one-dimensional spectrum obtained by integrating $F(f, \theta)$ over all directions. Thus

$$A_1 = \frac{Q_{12}}{[C_{11}(C_{22} + C_{33})]^{1/2}}, \quad B_1 = \frac{Q_{13}}{[C_{11}(C_{22} + C_{33})]^{1/2}},$$

$$A_2 = \frac{C_{22} - C_{33}}{C_{22} + C_{33}}, \qquad B_2 = \frac{2C_{23}}{C_{22} + C_{33}}. \qquad \text{(A3)}$$

In the above we make use of the relation

$$\left(\frac{C_{11}}{C_{22} + C_{33}}\right)^{1/2} = \frac{(2\pi f)^2}{k} = 1, \qquad \text{(A4)}$$

which is the dispersion relation for waves of small amplitude in deep water. The quantity $R = [C_{11}/(C_{22} + C_{33})]^{1/2}$ provides a check on the correct functioning of the wave buoy system and on the analysis.

If we assume a unimodal directional distribution, then two statistical parameters describing the mean wave direction θ_1 towards which the energy is traveling and angular spread θ_2 may be derived (Cartwright, 1963). That is

$$\theta_1 = \tan^{-1}(B_1/A_1),$$

$$\theta_2 = [(2 - 2C_1)]^{1/2} \quad \text{where} \quad C_1^2 = A_1^2 + B_1^2. \qquad \text{(A5)}$$

For a narrow directional distribution, θ_2 is equal to the rms angular spread about the mean wave direction.

Finally we define the spreading function $G(f, \theta)$ by

$$F(f, \theta) = G(f, \theta) \cdot E(f), \qquad \text{(A6)}$$

where $E(f)$ is the one-dimensional wave spectrum and

$$\int_0^{2\pi} G(f, \theta) d\theta = 1. \qquad \text{(A7)}$$

REFERENCES

Bendat, J. S., and A. G. Piersol, 1971: *Random Data: Analysis and Measurement Procedures,* Wiley-Interscience, 407 pp.

Cartwright, D. E., 1963: The use of directional spectra in studying the output of a wave recorder on a moving ship. *Ocean Wave Spectra.* Prentice-Hall, 203–218.

Cavanié, A. G., 1980: Evaluation of the standard error in the estimation of mean and significant wave heights as well as mean period from recordings of finite length. *Climatologie de la Mer; Sea Climatology.* Editions Technip, Paris, 73–88.

Ewing, J. A., and E. G. Pitt, 1982: Measurements of the directional wave spectrum off South Uist. *Wave and Wind Directionality: Applications to the Design of Structures.* Editions Technip, Paris, 47–63.

Guest, P. S., and K. L. Davidson, 1984: R/V *Polar Queen* atmospheric boundary layer measurements. *MIZEX Bull.,* **5,** 98–99.

Johannessen, O. M., and D. A. Horn, 1984: MIZEX: A program for mesoscale air–ice–ocean interaction experiments in Arctic marginal ice zones, MIZEX-84 Summer experiment PI preliminary reports. *MIZEX Bulletin V,* Johannessen and Horn, Eds., CRREL Special Rep. 84-29, Cold Regions Research and Engineering Laboratory, 176 pp.

Lawson, L. M., and R. B. Long, 1983: Multi-modal properties of the surface wave field observed with pitch–roll buoys during GATE. *J. Phys. Oceanogr.,* **13,** 474–486.

Long, R. B., 1980: The statistical evaluation of directional spectrum estimates derived from pitch–roll buoy data. *J. Phys. Oceanogr.,* **10,** 944–952.

——, 1985: Inverse modeling in ocean wave studies. *Wave Dynamics and Radio Probing of the Ocean Surface,* O. M. Phillips, Ed., In press.

——, and K. Hasselmann, 1979: A variational technique for extracting directional spectra from multi-modal wave data. *J. Phys. Oceanogr.,* **9,** 373–381.

Longuet-Higgins, M. S., 1977: The mean forces exerted by waves on floating or submerged bodies with applications to sand bars and wave power machines. *Proc. R. Soc., London,* **A352,** 463–480.

——, D. E. Cartwright and N. D. Smith, 1963: Observations of the directional spectrum of sea waves using the motions of a floating buoy. *Ocean Wave Spectra,* Prentice-Hall, 111–136.

Martin, S., P. Kauffman and C. Parkinson, 1983: The movement and decay of ice edge bands in the winter Bering Sea. *J. Geophys. Res.,* **88**(C5), 2803–2812.

Phillips, O. M., 1980: *The Dynamics of the Upper Ocean.* Cambridge University Press, 2nd ed., 336 pp.

Squire, V. A., 1983: Numerical modeling of realistic ice floes in ocean waves. *Ann. Glaciol.,* **4,** 277–282.

——, 1984: On the critical angle for ocean waves entering shore fast ice. *Cold Regions Sci. Technol.,* **10,** 59–68.

Wadhams, P., 1973: The effect of a sea ice cover on ocean surface waves. Ph.D. dissertation, University of Cambridge, 223 pp.

——, 1975: Airborne laser profiling of swell in an open ice field. *J. Geophys. Res.,* **80,** 4520–4528.

——, 1978: Wave decay in the marginal ice zone measured from a submarine. *Deep Sea Res.,* **25,** 23–40.

——, 1983: A mechanism for the formation of ice edge bands. *J. Geophys. Res.,* **88**(C5), 2813–2818.

——, 1985: The Marginal Ice Zone Experiment (MIZEX) 1984: Scott Polar Research Institute participation. *Polar Record,* **22**(140), 505–510.

——, 1986: The seasonal ice zone. *Sea Ice Geophysics,* N. Untersteiner, Ed., NATO Advanced Study Institute, Ser. C, Math. and Phys. Sciences, Reidel, In press.

——, V. A. Squire, J. A. Ewing and R. W. Pascal, 1985: Directional wave spectra measured near ice edges. *POAC-85, Proc. Eighth Int. Conf. on Port and Ocean Engineering under Arctic Conditions,* Narssarssuaq, Greenland, 7–14 September 1985, **1,** 326–338.

Weitz, M., and J. B. Keller, 1950: Reflection of water waves from floating ice in water of finite depth. *Commun. Pure Appl. Math.,* **3,** 305–318.